

JGR Solid Earth

RESEARCH ARTICLE

10.1029/2021JB021683

Key Points:

- Single-crystal elastic properties of omphacite were measured for the first time at high P-T conditions
- Undeformed eclogite is seismically invisible at 210–300 and 400–500 km depth range
- Modeled seismic anisotropy of deformed eclogite can be as high as 4%–5% in the uppermost mantle

Supporting Information:

Supporting Information may be found in the online version of this article.

Correspondence to:

M. Hao and J. S. Zhang,
minghao@unm.edu;
jinzhang@unm.edu




Citation:

Hao, M., Zhang, J. S., Zhou, W.-Y., & Wang, Q. (2021). Seismic visibility of eclogite in the Earth's upper mantle—Implications from high pressure-temperature single-crystal elastic properties of omphacite. *Journal of Geophysical Research: Solid Earth*, 126, e2021JB021683. <https://doi.org/10.1029/2021JB021683>

Received 9 JAN 2021

Accepted 5 APR 2021

Seismic Visibility of Eclogite in the Earth's Upper Mantle—Implications From High Pressure-Temperature Single-Crystal Elastic Properties of Omphacite

Ming Hao^{1,2} , Jin S. Zhang^{1,2} , Wen-Yi Zhou^{1,2} , and Qin Wang³ 

¹Department of Earth and Planetary Sciences, University of New Mexico, Albuquerque, NM, USA, ²Institute of Meteoritics, University of New Mexico, Albuquerque, NM, USA, ³School of Earth Sciences and Engineering, Nanjing University, Nanjing, China

Abstract Identifying and locating the geochemical and geophysical heterogeneities in the Earth's interior is one of the most important and challenging tasks for the deep Earth scientists. Subducted oceanic crust metamorphizes into the dense eclogite in the upper mantle and is considered as a major cause of geochemical and geophysical heterogeneities in the deep Earth. In order to detect eclogitic materials inside the Earth, precise measurements of the high pressure-temperature single-crystal elasticity of major minerals in eclogite are thus exceedingly important. Omphacite, a Na,Al-bearing clinopyroxene, constitutes up to 75 vol% of eclogite. In the present study, we performed the first high pressure-temperature single-crystal elasticity measurements of omphacite using Brillouin spectroscopy. Utilizing the finite-strain approach, we obtained the following thermoelastic parameters for omphacite: $K_{S0}' = 4.5(1)$, $G_0' = 1.53(5)$, $\partial K_{S0}'/\partial T = -0.029(5)$ GPa/K, $\partial G_0'/\partial T = -0.013(5)$ GPa/K, with $K_{S0} = 123(3)$ GPa, $G_0 = 74(2)$ GPa, and $\rho_0 = 3.34(1)$ g/cm³. We found that the seismic velocities of undeformed eclogite are similar to pyrolite at the depths of 200–300 and 410–500 km, thus eclogite is seismically invisible at these depths. Combined with the lattice-preferred orientations of the omphacite in naturally deformed eclogites, we also modeled seismic anisotropy of eclogite at various pressure-temperature conditions. A 10 km thick subducted eclogitic crust can result in ~ 0.2 s shear wave splitting in the Earth's upper mantle.

Plain Language Summary Omphacite, as a type of clinopyroxene, is one of the main mineral phases in the deeply sinking basaltic materials recycled to the deep Earth. To better constrain seismic properties of the subducted oceanic crust, we experimentally measured elastic properties of omphacite under high pressure-temperature conditions. Using our results, the calculated seismic anisotropy of deformed basaltic oceanic crust is on the level of 4%–5% in the uppermost mantle. If the subducted basaltic materials remained undeformed, their isotropic seismic velocities are identical to the ambient mantle at depths between 200–300 and 410–500 km.

1. Introduction

The Earth's oceanic crust is primarily made of basalt. When the oceanic lithosphere is subducted, the basaltic oceanic crust metamorphizes into eclogite when the pressure and temperature exceed 2 GPa and 1073 K (Ito & Kennedy, 1971). Due to its high density, the formation of eclogite further helps the slab subduction (Moghadam et al., 2010; Xu et al., 2008). Omphacite, the solid solution of diopside (CaMgSi₂O₆) and jadeite (NaAlSi₂O₆), is the major mineral phase in eclogite (up to 75 vol%) and can stably exist at depths up to 500 km. Due to the slow mixing and diffusion process within the Earth's interior, the recycled eclogitic materials can be preserved over the geological time as chemical heterogeneities in the deep Earth (Ballmer et al., 2017; Xu et al., 2008). To seismically identify those heterogeneities, the high pressure-temperature elastic properties of relevant minerals are needed.

Seismologists have found complex seismic anisotropy features near subduction zones (e.g., Long & Silver, 2008; Niday & Humphreys, 2020), which are generally explained as the result of the flow-induced lattice-preferred orientation (LPO) of the elastically anisotropic minerals. Understanding the seismic anisotropy observations as well as the mantle flow field requires knowledge of the single-crystal elasticity and the LPO of relevant minerals, such as omphacite in the subducted slab crust.

Although the elastic properties of the Ca,Mg endmember of clinopyroxene, diopside, have been thoroughly investigated (e.g., Isaak et al., 2006; Li & Neuville, 2010; Sang & Bass, 2014; Sang et al., 2011; Walker, 2012), the single-crystal elastic properties of omphacite, on the other hand, are less constrained. High-pressure single-crystal elasticity studies of omphacite are either performed at 0 K condition computationally (Skeltson & Walker, 2015), or measured at 300 K condition experimentally (Hao et al., 2019). Our ability to trace the eclogitic materials in the deep Earth through seismic methods is substantially restricted by the lack of knowledge on the temperature-dependent single-crystal elasticity of omphacite at high-pressure condition. Thus, building up on our previous high-pressure study on omphacite single crystals at 300 K (Hao et al., 2019), we further conducted single-crystal Brillouin spectroscopy experiments on the same crystals at simultaneously high pressure-temperature conditions up to 18 GPa and 700 K, and then modeled the isotropic and anisotropic seismic properties of the undeformed and deformed eclogite samples after combining the laboratory determined LPO with the updated pressure-temperature dependent single-crystal elastic properties of omphacite. The results presented in this study will serve as the basis for detecting the recycled oceanic crust in the Earth's upper mantle.

2. Experiments

The omphacite crystals we utilized in this study are the same as the ones used in Hao et al. (2019), with the chemical composition of $\text{Na}_{0.289}\text{Mg}_{0.633}\text{Ca}_{0.68}\text{Fe}_{0.108}\text{Al}_{0.323}\text{Si}_{1.975}\text{O}_6$ determined by Electron Microprobe (EPMA). The selected crystals were hand-polished to 10–20 μm thick platelets using aluminum oxide lapping films. They are optically examined to be scratch-free and inclusion-free under the microscope. The crystals were then cut into smaller pieces with lateral dimensions between 40 and 60 μm for the diamond anvil cell (DAC) loading. The plane normals of different crystals were measured at 13-BM-D station of GeoSoilEnviroCARS (GSECARS). The technical details of the X-ray diffraction experiments for determining the crystal orientations can be found in Hao et al. (2019). The face normals of the polished crystals are: $(-0.152, -0.969, 0.195)$, $(0.242, 0.299, -0.923)$, and $(0.651, -0.759, -0.005)$. The angular uncertainties are $1\text{--}2^\circ$. Based on the sensitivity test (Text S1.1) result shown in Figure S1, the sound velocity measurements within the three selected crystal platelets could offer enough constraints for the 13 independent single-crystal elastic moduli (C_{ij} s) of the monoclinic omphacite.

We used resistively heated DACs for generating the high pressure-temperature conditions. A pair of 16-sided standard-cut diamond anvils with 450 μm cutlets were glued to two 90° opening standard WC seats, and then placed in a BX90 DAC (Kantor et al., 2012). The sample chamber was formed by the two diamond anvils and a ~ 50 μm thick pre-indented Re foil with a ~ 280 μm diameter hole. A Pt heater, which is made of a pyrophyllite ring base with three equal-length Pt wires (Lai et al., 2020), was placed between the two WC seats to heat up the sample chamber at high-pressure conditions. Two K-type thermocouples were placed in direct contact with the diamond on the same side, and as close as possible to the diamond culet. Additional cement was added on top of the conjunctions to insulate the thermocouples from the Pt heater. In addition, we filled the space within the DAC as well as the space between the DAC and the water-cooled Al DAC holder with high-temperature ceramic fiber, which also helped reduce the heat loss and the temperature gradient within the DAC. Figure S2 shows the power curve of the high pressure-temperature experiments, the power at the 700 K is about 85 W. The maximum difference between the temperature readings from the two thermocouples was ~ 8 K throughout the entire examined pressure-temperature range. We did not use any inert gas to protect the diamonds due to the relatively low temperature reached in this study. None of the diamonds used in this study showed any oxidation/heat damage after the experiments. The DAC sample chambers were filled with a Neon pressure-transmitting medium using GSECARS's gas loading system (Rivers et al., 2008). Two ruby spheres were loaded with the crystal inside the DAC sample chamber and ruby fluorescence shift measurements were employed for pressure determination (Datchi et al., 2007; Shen et al., 2020). We estimated pressure uncertainties from the temperature difference of the two thermocouples and the two pressure readings before and after each Brillouin experimental run.

We conducted all high pressure-temperature Brillouin spectroscopy measurements in the UNM laser spectroscopy laboratory. The spectroscopy system is equipped with a 300 mW 532 nm single-mode Spectra Physics diode-pumped solid-state laser, and a six-pass tandem Fabry-Perot interferometer with Hamamatsu H10682 detector. We use a line polarizer to adjust the laser beam power. The power reaching the DACs

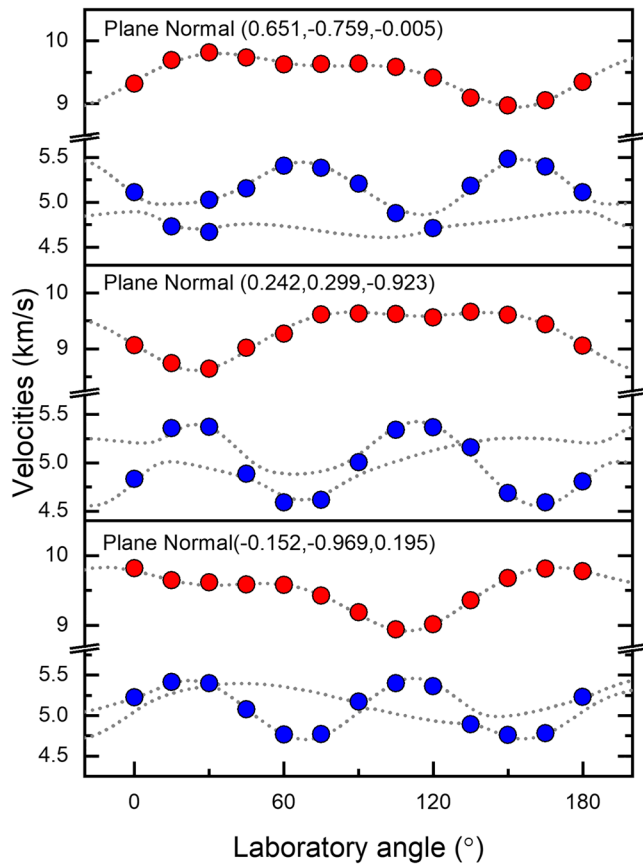


Figure 1. Experimentally determined velocities of the omphacite crystals with different orientations at 18.4 GPa and 700 K. The dotted lines are calculated from the final C_{ij} model, and the circles represent the measured velocities. The phonon directions of the V_p and V_s measurements were calculated by matching the in-plane measured velocities with velocity dispersion curves predicted by the best-fit C_{ij} model. The uncertainties of the individual velocity measurements are smaller than the symbols. The root-mean-square (RMS) error between the experimental data and the model is 35 m/s.

is ~ 80 – 100 mW. The incoming laser is focused onto the sample with a 9 mm diameter MgF_2 coated plano-convex lens with a focal length of 36 mm and the Brillouin scattered light is collected by a 30 mm diameter achromat with a focal length of 100 mm. The detailed experimental setup has been described in Zhang et al. (2015). The silica glass Corning 7980 is used to calibrate the scattering angle for the 50° scattering geometry, resulting in a scattering angle of $50.68(6)^\circ$ (Zhang et al., 2011). We were able to observe both the shear (V_s) and compressional (V_p) modes in all Brillouin spectra we collected at 13 different Chi angles ($360, 345, 315, 285, 255, 225, 195, 180, 150, 120, 90, 60, 30$) along the 360° azimuth for all three crystals at each pressure-temperature condition to avoid any geometrical errors. A typical high pressure-temperature Brillouin spectrum was shown in Figure S3 with a collection time of ~ 7 min.

3. Results and Discussion

The elastic properties of omphacite at ambient condition ($\rho_0 = 3.34(1)$ g/cm³, $K_{S0} = 123(3)$ GPa, $G_0 = 74(2)$ GPa) were adopted from Hao et al. (2019) and fixed in the following inversion process. The high pressure-temperature thermoelastic parameters of omphacite were iteratively calculated using the high pressure-temperature data obtained in this study combined with the room-temperature high-pressure data from Hao et al. (2019). Given as a starting single-crystal C_{ij} model with hypothetical high pressure-temperature densities, we calculated the C_{ij} s, K_S , G , V_s , and V_p at each pressure-temperature condition through the least squares inversion of the Christoffel equation. In this step, only V_s and V_p represent the true high pressure-temperature values, since they are independent of the assumed density. We then fit the temperature-dependent third order finite-strain equation of state to the true V_s - V_p -pressure-temperature data set to acquire the true high pressure-temperature densities, and the pressure and temperature derivatives of G and K_S (Davies & Dziewonski, 1975; Duffy & Anderson, 1989). The last step is to update the C_{ij} s, G , and K_S , with true densities at high pressure-temperature condition. The actual measurements at 18.4 GPa 700 K and the velocities calculated from the final C_{ij} model are plotted together in Figure 1. Table 1 lists the density, V_s , V_p , C_{ij} s, G , K_S , and G under each pressure-temperature condition. Table S1 shows the trade-off coefficients of the 13 independent C_{ij} s at 3.8 GPa and 400 K.

The K_{S0} , G_0 , $\partial K_{S0}/\partial T$, and $\partial G_0/\partial T$ were determined to be 4.5(1), 1.53(5), $-0.029(5)$ GPa/K, and $-0.013(5)$ GPa/K, respectively, with fixed $K_{S0} = 123(3)$ GPa, $G_0 = 74(2)$ GPa, and $\rho_0 = 3.34(1)$ g/cm³. We used the thermal expansion coefficient $\alpha_0 = 2.7(8) \times 10^{-5}$ K⁻¹ for omphacite (Hao et al., 2019), and the K_{S0} and G_0 calculated using the high pressure-temperature data set in this study are consistent with previous high-pressure ambient-temperature experiments on the same crystals (Hao et al., 2019). Figure 2 and Figure S4 shows the G , K_S , V_s , and V_p of the sample under high pressure-temperature conditions. Li and Neuville (2010) conducted ultrasonic acoustic measurements at high pressure-temperature conditions for diopside, and obtained $K_{S0} = 116.4(7)$ GPa, $K_{S0}' = 4.9(1)$, $\partial K_{S0}/\partial T = -0.012(1)$ GPa/K, $G_0 = 73.0(4)$ GPa, $\partial G_0/\partial T = -0.011(1)$ GPa/K. Compared with the values determined for diopside (Li & Neuville, 2010), the K_{S0} and G_0 of omphacite measured in this study are higher than diopside as expected, whereas the pressure derivatives are lower. On the other hand, the temperature derivatives of K_{S0} and G_0 of omphacite are higher than diopside. Therefore, higher jadeite component in clinopyroxene decreases the pressure dependence but increases the temperature dependence of the elastic moduli.

Figure 2 shows the first experimentally measured C_{ij} s and the finite strain fitting results for omphacite at high pressure-temperature conditions. All the diagonal C_{ij} s, C_{12} , and C_{13} decrease with temperature.

Table 1
Density, C_{ij} s, K , G , V_p , and V_s of Omphacite at Each Pressure-Temperature Condition Determined in This Study

	1.4(1) GPa 400 K	3.8(1) GPa 400 K	10.0(1) GPa 400 K	14.8(1) GPa 400 K	17.0(1) GPa 400 K	4.3(3) GPa 500 K	10.9(2) GPa 500 K
ρ (g/cm ³)	3.369	3.432	3.579	3.679	3.722	3.436	3.591
ρ^* (g/cm ³)	3.369(10)	3.432(10)	3.580(10)	3.681(10)	3.725(10)	3.436(10)	3.591(10)
C ₁₁ (GPa)	237.9(6)	255(1)	296.1(7)	329.2(9)	341(1)	253(1)	297.8(7)
C ₂₂ (GPa)	201.1(9)	208(2)	241.7(9)	263(1)	275(2)	208(1)	241(1)
C ₃₃ (GPa)	258.2(6)	277(1)	312.4(9)	340.8(7)	352(1)	277.1(9)	313(1)
C ₄₄ (GPa)	78.8(4)	83.2(6)	87.6(6)	91.5(7)	93(1)	82.9(6)	87.9(7)
C ₅₅ (GPa)	68.9(4)	70.8(6)	79.1(4)	83.0(4)	84.8(6)	71.1(6)	78.5(4)
C ₆₆ (GPa)	75.4(3)	81.3(7)	96.1(4)	107.4(7)	112.2(8)	80.2(6)	95.3(5)
C ₁₂ (GPa)	85.3(7)	94(1)	118.6(8)	139(1)	145(1)	94(1)	120(1)
C ₁₃ (GPa)	75.6(7)	82(1)	103.2(9)	122(1)	132(1)	81(1)	104(1)
C ₂₃ (GPa)	62(2)	76(2)	93(3)	107(2)	111(3)	68(2)	92(3)
C ₁₅ (GPa)	8.4(4)	7.7(6)	6.8(4)	3.4(5)	4.7(8)	7.7(6)	5.3(4)
C ₂₅ (GPa)	8.0(9)	7(1)	5.4(8)	8(1)	9(2)	4(1)	6.2(9)
C ₃₅ (GPa)	34.6(4)	34.5(6)	25.5(5)	23.1(5)	21.6(7)	32.4(6)	27.8(5)
C ₄₆ (GPa)	7.1(3)	5.1(6)	4.8(4)	6.8(7)	1.3(9)	6.0(6)	7.0(5)
K _S ^R (GPa)	121.8(4)	133.1(7)	160.9(7)	181.2(6)	189.2(8)	131.6(6)	160.9(8)
G ^R (GPa)	73.3(2)	76.6(3)	85.9(3)	91.2(3)	94.0(4)	76.8(3)	85.3(3)
K _S ^V (GPa)	127.0(4)	138.1(7)	164.5(7)	185.3(6)	193.5(8)	135.9(6)	164.9(8)
G ^V (GPa)	76.2(2)	79.6(3)	88.2(3)	94.1(3)	96.6(4)	79.8(3)	88.1(3)
K _S ^{VRH} (GPa)	124(3)	136(3)	163(2)	183(2)	191(3)	134(3)	163(3)
G ^{VRH} (GPa)	75(2)	78(2)	87(1)	93(2)	95(2)	78(2)	87(2)
V _p (km/s)	8.16(4)	8.36(4)	8.83(3)	9.13(3)	9.25(3)	8.33(3)	8.81(3)
V _s (Km/s)	4.71(3)	4.77(3)	4.93(2)	5.02(2)	5.06(2)	4.77(3)	4.91(2)
	14.9(2) GPa 500 K	16.9(2) GPa 500 K	2.7(4) GPa 700 K	11.5(4) GPa 700 K	14.9(4) GPa 700 K	18.4(3) GPa 700 K	
ρ (g/cm ³)	3.673	3.713	3.374	3.587	3.658	3.727	
ρ^* (g/cm ³)	3.674(10)	3.713(10)	3.374(10)	3.586(10)	3.658(10)	3.726(10)	
C ₁₁ (GPa)	327(1)	337(1)	233(1)	293(1)	319(1)	341.1(8)	
C ₂₂ (GPa)	258(1)	270(1)	196(2)	237(2)	255(2)	272(1)	
C ₃₃ (GPa)	337.5(9)	345(1)	251(1)	304(1)	335(1)	348.7(7)	
C ₄₄ (GPa)	89.8(7)	92.8(9)	75.4(7)	86.2(9)	88(1)	92.6(8)	
C ₅₅ (GPa)	81.8(5)	84.4(5)	68(1)	77.1(6)	79.5(5)	84.8(4)	
C ₆₆ (GPa)	105.5(7)	110.6(7)	71.5(6)	93.4(7)	103.3(8)	109.5(5)	
C ₁₂ (GPa)	137(1)	142(1)	81(1)	114(1)	132(1)	143.9(8)	
C ₁₃ (GPa)	118(1)	128(1)	71(1)	100(1)	117(1)	128.5(9)	
C ₂₃ (GPa)	110(3)	115(3)	61(3)	94(4)	99(3)	117(2)	
C ₁₅ (GPa)	3.0(7)	5.3(7)	9.2(7)	5.7(7)	4.0(7)	6.0(5)	
C ₂₅ (GPa)	10(1)	13(1)	7(1)	10(1)	13(1)	14.1(9)	
C ₃₅ (GPa)	21.7(6)	21.6(7)	33.0(8)	30.0(8)	18.8(7)	19.8(4)	
C ₄₆ (GPa)	3.4(7)	0.5(6)	7.4(7)	6.2(7)	1.0(8)	2.5(6)	
K _S ^R (GPa)	179.8(7)	186.8(7)	118.1(8)	157(1)	173.5(8)	188.7(5)	
G ^R (GPa)	89.8(3)	92.7(4)	71.5(4)	83.9(4)	88.9(4)	93.1(3)	
K _S ^V (GPa)	183.9(7)	191.4(7)	122.9(8)	161(1)	178.2(8)	193.4(5)	

Table 1
Continued

	14.9(2) GPa 500 K	16.9(2) GPa 500 K	2.7(4) GPa 700 K	11.5(4) GPa 700 K	14.9(4) GPa 700 K	18.4(3) GPa 700 K
G^V (GPa)	92.6(3)	95.4(4)	74.2(4)	86.4(4)	91.5(4)	95.5(3)
K_S^{VRH} (GPa)	182(3)	189(3)	121(3)	159(3)	176(3)	191(3)
G^{VRH} (GPa)	91(2)	94(2)	73(2)	85(2)	90(2)	94(2)
V_p (km/s)	9.09(3)	9.21(3)	8.06(4)	8.72(3)	9.00(3)	9.22(3)
V_s (Km/s)	4.98(2)	5.04(2)	4.67(3)	4.87(2)	4.97(2)	5.03(2)

Notes. The Reuss and Voigt bounds of the homogeneous isotropic aggregate under the VRH averaging scheme are denoted by the superscripts R and V. The density values obtained using the temperature dependent finite-strain equation of state derived from the V_p - V_s -pressure-temperature data set in this study are reported as ρ , and for comparison, the density values calculated using the thermal equation of state in Hao et al. (2019) are presented as ρ^* .

However, the temperature effects on C_{23} , C_{15} , C_{25} , C_{35} , and C_{46} are less significant, especially considering the relatively large uncertainties of C_{15} , C_{25} , and C_{46} . Isaak et al. (2006) measured the single-crystal elastic properties of diopside up to 1300 K at ambient pressure and found that C_{15} , C_{25} , and C_{46} are the only C_{ij} s increasing with temperature. The results in this study are consistent with what were found by Isaak et al. (2006).

4. Implications

Subducted or delaminated basaltic materials are important geophysical and geochemical heterogeneities in the deep Earth (Xu et al., 2008). Better constrained seismic properties of basaltic materials help us in identifying the possibly eclogite-rich regions in the deep Earth. In the following sections, we will focus on modeling both the seismic anisotropy and the isotropic seismic velocities of eclogite aggregates.

4.1. Seismic Anisotropy of Deformed Eclogite in the Subducted Slab Crust

The stresses in a subducting slab are controlled by tectonic forces, and the subducted slab crust which is adjacent to the slab-mantle interface, is likely to experience extreme stress during subduction. As a result, the eclogite formed under these conditions is expected to be strongly deformed depending on the subduction speed and geometry (Royden & Husson, 2006). Therefore, we need to combine the pressure-temperature dependent single-crystal elasticity with the rock textures (in particular, the LPO of omphacite) to derive the anisotropic seismic properties of the subducted and deformed slab crust.

Wang et al. (2009) measured the LPO of naturally deformed eclogite samples from the Sulu ultrahigh-pressure metamorphic terrane. These eclogite samples are believed to originate from >125 km depth, and thus are likely to represent the subducted basaltic rocks which were quickly exhumed to the upper crust afterward. Wang et al. (2009) found that even though garnet, which is nearly elastically isotropic (Sinogeikin & Bass, 2000), is the volumetrically more abundant phase in some of their samples (up to 87 vol%), omphacite dominates seismic anisotropy of eclogite. This is consistent with the results shown in Kim et al. (2018). During the subduction, the LPO of anisotropic omphacite induced by ductile deformation is the main contributor to seismic anisotropy of the subducted basaltic rocks in the upper mantle (e.g., Zhang et al., 2006). Therefore, estimating the seismic anisotropies of deformed omphacite at elevated pressure-temperature conditions is essential for interpreting seismic anisotropy near subduction zones.

Combining the experimentally determined single-crystal C_{ij} s with microstructure of naturally deformed eclogite, seismic anisotropy caused by the LPO of omphacite can be modeled at elevated pressure-temperature conditions. Using the MTEX software package (Mainprice et al., 2011) and the electron backscatter diffraction (EBSD) measurements of eclogite by Wang et al. (2009), we modeled the V_s polarization anisotropy D^{Vs} , V_p , V_{s1} , and V_{s2} distributions of omphacite for two naturally deformed eclogite samples B270 and B295 (Supporting Information, Equations S2–S5). The calculated pole figures of sample B270 and B295 are shown in Figure 3 and Figure S5, respectively. The overall textures of the two samples are similar, although sample B270 shows higher anisotropy. It is worth noting that seismic anisotropy of B295 calculated in Wang et al. (2009) is different from the results in this study, which is due to the use of different C_{ij} models

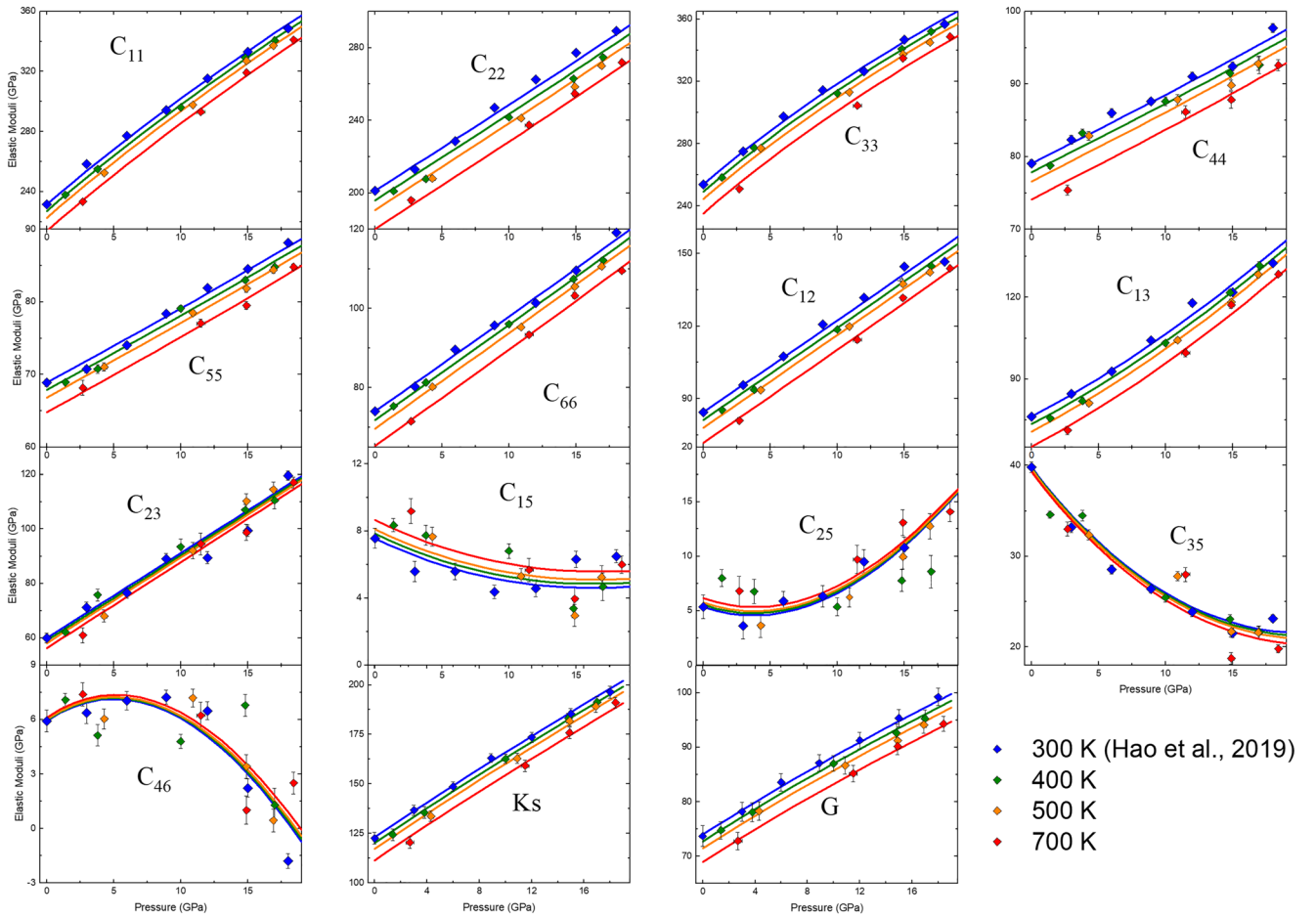


Figure 2. The high pressure-temperature C_{ij} s, K_s , and G of omphacite determined in this study. The blue, green, orange, and red solid lines represent the finite strain fitting results at 300, 400, 500, and 700 K, respectively.

of omphacite. Wang et al. (2009) utilized the C_{ij} s of a jadeite-rich omphacite sample measured at ambient condition by Bhagat et al. (1992), whereas we employ the high pressure-temperature C_{ij} s of a diopside-rich omphacite sample from this study. With relatively weaker fabrics in sample B295, the use of different C_{ij} models has a strong impact on its overall calculated seismic anisotropy. The discussion below is based on the modeling results of sample B270 which shows a stronger texture than B295.

As shown in Figure 3, the fastest V_p direction of sample B270 is always subparallel to the lineation and the slowest V_p direction is subnormal to the foliation. The V_p anisotropy clearly increases with temperature and decreases with pressure. At relatively low pressure-temperature conditions (6 GPa and 1000 K), the V_p anisotropy of omphacite is $\sim 7.2\%$. Considering the omphacite volume fraction of $\sim 70\%$ and the random orientation of the nearly isotropic garnet (Kim et al., 2018; Sinogeikin & Bass, 2000; Wang et al., 2009) in eclogite, the V_p anisotropy of eclogite is on the order of 5% – 6% in the shallower upper mantle. When reaching ~ 14 GPa and 1800 K at transition zone depths, the V_p anisotropy of omphacite increases to 8.2% . However, considering that the volume fraction of omphacite decreases from $\sim 70\%$ at the top of the upper mantle to $\sim 20\%$ in the transition zone (Aoki & Takahashi, 2004), the V_p anisotropy of eclogite would be only at the level of $\sim 2\%$ in the transition zone.

The D^{Vs} pole figures are complex. At lower pressures, the direction with lowest D^{Vs} is subparallel to the lineation and the direction with highest D^{Vs} is sub-perpendicular to the lineation and subparallel to the foliation direction. However, at higher pressures, the directions with the lowest D^{Vs} appear both along the lineation and perpendicular to the foliation direction. Temperature does not affect the overall shape of the pole figures of D^{Vs} , although temperature does increase the strength of seismic anisotropy.

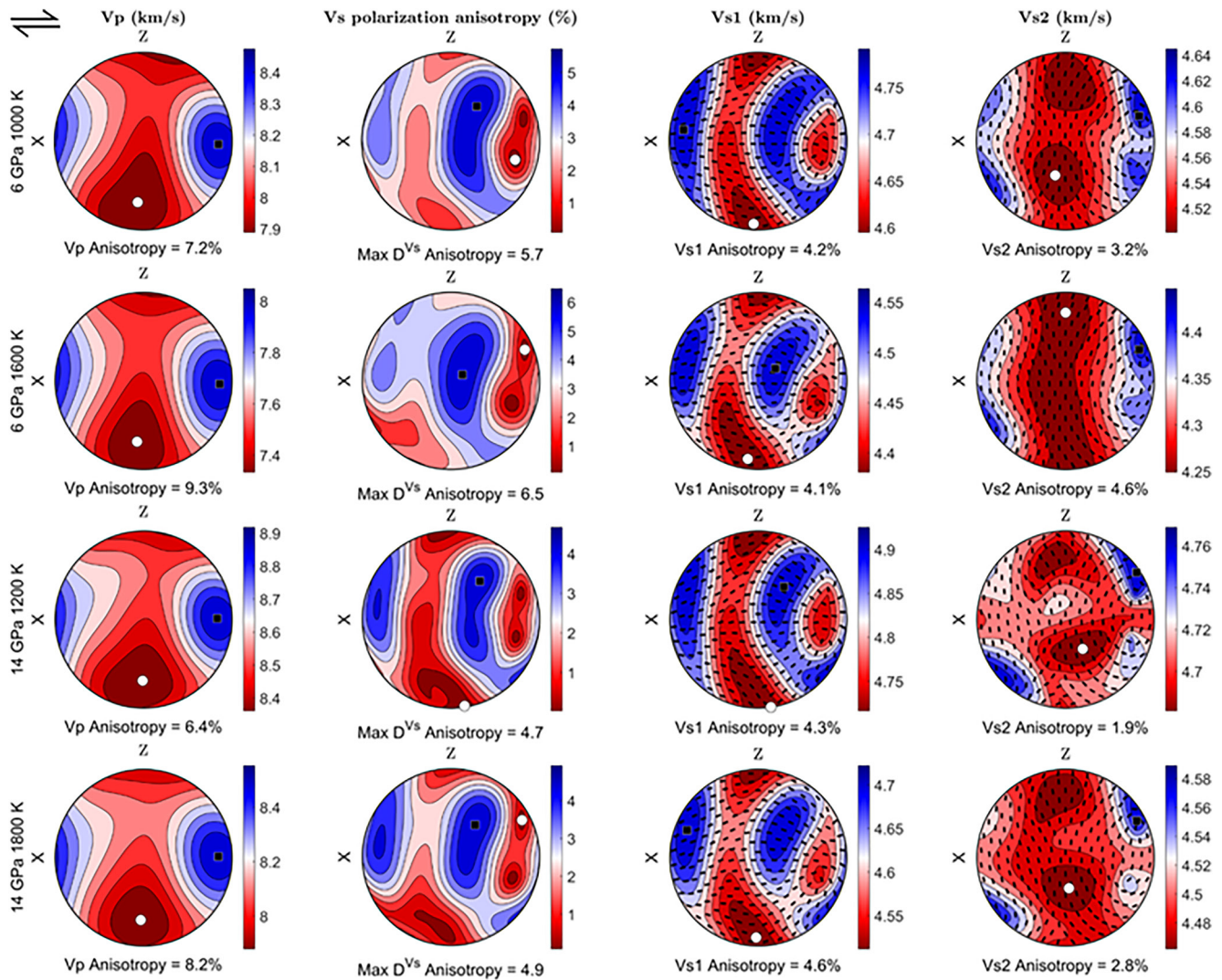


Figure 3. Calculated seismic anisotropy of omphacite in deformed eclogite sample B270 at high pressure-temperature conditions (Wang et al., 2009). Equal area projection, lower hemisphere. The direction perpendicular to the foliation (Z) is shown vertical and the lineation (X) is horizontal. The black square and white circle mark the highest and lowest values, respectively, in each pole figure. Vs1 presents the fast Vs and the black bars are the polarization directions of Vs.

Mantle flow geometries near a subducting slab are complicated. Near the slab wedge, there are two dominating mantle flow fields: the 2-D corner flow is along the dipping direction and perpendicular to the trench, and the 3-D around flow is parallel to the trench (Figure S6, Eakin et al., 2010; Long & Silver, 2008). Different mantle flow patterns will produce different shear directions at the slab-mantle interface, and thus affect the lineation of the deformed eclogite in the subducted crust. In this study, we assumed a seismic ray with nearly normal incidence, similar to what is expected in the SKS splitting measurements. For the 2-D corner flow, the fast Vs polarization of the deformed eclogite will be perpendicular to the trench with a small dipping angle, or parallel to the trench with a high dipping angle. The 3-D around flow always results in fast Vs polarization parallel to the trench and the dipping angle does not matter. Considering the fact that garnet is nearly isotropic and does not show clear LPO in the deformed eclogite (Sinogeikin & Bass, 2000; Kim et al., 2018), the shear wave splitting of the subducted oceanic crust is primarily caused by the LPO of omphacite. According to Figure 3, a 10 km thick subducted eclogitic crust can lead to ~0.2 s shear wave splitting in the upper mantle, which cannot be ignored when interpreting seismic data in subduction zones (Eakin et al., 2010; Niday & Humphreys, 2020).

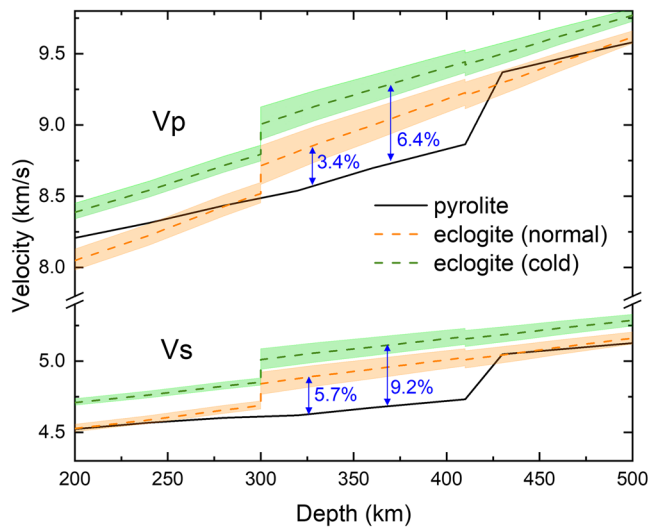


Figure 4. Seismic velocities of undeformed eclogite determined in this study and pyrolite shown in Xu et al. (2008). The shaded green and orange regions represent the Voigt and Reuss bounds along the normal (1600 K) and cold (1000 K) geotherms, respectively.

4.2. Isotropic Seismic Velocities of Undeformed Eclogite

In addition to the slab crust, the lower continental crust is also believed to be compositionally basaltic (Wedepohl, 1995). Delamination of the basaltic continental lower crust is another way to recycle shallow materials down to the deep Earth (Kay & Mahlburg-Kay, 1991). Weaker stress fields are associated with the delamination processes compared to subduction zones, and eclogite involved in the delamination process is less likely to form strong deformation textures. It is thus worth to reevaluate the isotropic seismic properties of eclogite as an end member case, based on the pressure-temperature dependent elastic properties of omphacite and other relevant mineral phases (Aoki & Takahashi, 2004; Table S2).

In this study, we considered two geotherm profiles at 200–500 km depth: one along the 1000 K mantle adiabat, and the other along the 1600 K adiabat (Katsura et al., 2010; Stixrude & Lithgow-Bertelloni, 2005), representing a cold and a normal mantle temperature conditions. We also compared the velocities of eclogite with those of the pyrolitic mantle (Xu et al., 2008), as shown in Figure 4 and Figure S7. We calculated the mineral compositions and proportions both as depth-dependent, and for solid solution we considered the simplest ideal mixing scenario. To calculate the elastic moduli and densities for the multi-component systems, we adopted the Voigt-Reuss-Hill averaging scheme (Text S1.3, Equation S6–S8). Instead of assuming all clinopyroxenes share the same temperature

dependence of elastic moduli and using previously determined values for diopside, we remodeled the seismic velocities of eclogite using the new thermoelastic parameters of omphacite determined in this study.

The new results showed $\sim 2\%$ slower seismic velocities of eclogite compared to what were calculated by Hao et al. (2019), although the maximum V_s and V_p differences still appear between ~ 300 and 410 km. Along normal geotherm, the V_s and V_p of eclogite are $\sim 5.7\%$ and $\sim 3.4\%$ higher than those of the pyrolitic mantle, respectively. The possible lower temperature of eclogite enhances the velocity contrast to $\sim 5.7\%$ – 9.2% and $\sim 3.4\%$ – 6.4% for V_s and V_p , respectively.

At depth shallower than 300 km or deeper than 410 km, the V_p and V_s of eclogite are practically indistinguishable from pyrolite. This is the major revision to what was found in Hao et al. (2019). The difference is caused by the use of diopside's $\partial K_{S0}/\partial T$ and $\partial G_0/\partial T$ for omphacite in the calculation in Hao et al. (2019). The temperature dependence of K_{S0} and G_0 of omphacite measured in this study are higher than diopside, resulting in lower V_p and V_s for the model eclogite calculated in this study. Our model suggests that the seismic anomalies observed at depth shallower than 300 km and deeper than 410 km are primarily caused by temperature variations rather than compositional heterogeneities due to recycled eclogite. In other words, eclogitic materials are seismically invisible at those depth ranges. Only when interpreting seismic observations of subduction zones at depth between 300 and 410 km depth, the composition-induced velocity differences need to be taken into consideration.

5. Conclusions

We have measured the single-crystal elastic properties of omphacite using Brillouin spectroscopy at simultaneously high pressure-temperature condition up to 18 GPa and 700 K. The new thermoelastic parameters of omphacite determined in this study are: $K_{S0} = 123(3)$ GPa, $G_0 = 74(2)$ GPa, $K_{S0}' = 4.5(1)$, $G_0' = 1.53(5)$, $\partial K_{S0}/\partial T = -0.029(5)$ GPa/K, and $\partial G_0/\partial T = -0.013(5)$ GPa/K. Combining the EBSD measurements of naturally deformed eclogite, we modeled seismic anisotropy of deformed eclogite at high pressure-temperature conditions. We found that the LPO of anisotropic omphacite can result in shear-wave splitting time of ~ 0.2 s for a 10 -km-thick eclogitic crust. The isotropic seismic velocities of undeformed eclogite are indistinguishable from the pyrolitic mantle at the depths between 200 – 300 and 410 – 500 km. As a result, the seismic anomalies observed at shallower upper mantle and the upper transition zone are primarily of thermal origin rather than caused by the compositional heterogeneities of eclogitic materials.

Data Availability Statement

The presented data can be found in the UNM digital data repository at https://digitalrepository.unm.edu/eps_fsp/10.

Acknowledgments

The authors would like to thank Jane Silverstone for providing the omphacite sample, Caroline E. Pierotti for polishing the samples, Mike Spilde for the help with EPMA measurements, Lowell Miyagi for the advice on anisotropy calculations, and Sergey Tkachev for the help in experiments at GSECARS as well as the Neon gas loadings. The use of the gas-loading system is supported by COMPRES, the Consortium for Materials Properties Research in Earth Sciences under NSF Cooperative Agreement EAR 1661511, and GSECARS are funded by NSF (EAR—1634415) and Department of Energy (DOE)—GeoSciences (DE-FG02-94ER14466). This research used resources of APS, a U.S. DOE Office of Science User Facility operated for the DOE Office of Science by Argonne National Laboratory under Contract NO. DE-AC02-06CH11357. This work is supported by the National Science Foundation (NSF) under Grant EAR 1646527 (JZ), EAR 1847707 (JZ) and the start-up fund from UNM (JZ).

References

- Aoki, I., & Takahashi, E. (2004). Density of MORB eclogite in the upper mantle. *Physics of the Earth and Planetary Interiors*, 143–144, 129–143. <https://doi.org/10.1016/j.pepi.2003.10.007>
- Ballmer, M. D., Houser, C., Hernlund, J. W., Wentzcovitch, R. M., & Hirose, K. (2017). Persistence of strong silica-enriched domains in the Earth's lower mantle. *Nature Geoscience*, 10(3), 236. <https://doi.org/10.1038/ngeo2898>
- Bhagat, S. S., Bass, J. D., & Smyth, J. R. (1992). Single-crystal elastic properties of omphacite-C2/c by Brillouin spectroscopy. *Journal of Geophysical Research*, 97(B5), 6843–6848. <https://doi.org/10.1029/92jb00030>
- Datchi, F., Dewaele, A., Loubeyre, P., Letoullec, R., Le Godec, Y., & Canny, B. (2007). Optical pressure sensors for high-pressure-high-temperature studies in a diamond anvil cell. *High Pressure Research*, 27(4), 447–463. <https://doi.org/10.1080/08957950701659593>
- Davies, G. F., & Dziewonski, A. M. (1975). Homogeneity and constitution of the Earth's lower mantle and outer core. *Physics of the Earth and Planetary Interiors*, 10(4), 336–343. [https://doi.org/10.1016/0031-9201\(75\)90060-6](https://doi.org/10.1016/0031-9201(75)90060-6)
- Duffy, T. S., & Anderson, D. L. (1989). Seismic velocities in mantle minerals and the mineralogy of the upper mantle. *Journal of Geophysical Research*, 94(B2), 1895–1912. <https://doi.org/10.1029/jb094ib02p01895>
- Eakin, C. M., Obrebski, M., Allen, R. M., Boyarko, D. C., Brudzinski, M. R., & Porritt, R. (2010). Seismic anisotropy beneath Cascadia and the Mendocino triple junction: Interaction of the subducting slab with mantle flow. *Earth and Planetary Science Letters*, 297(3–4), 627–632. <https://doi.org/10.1016/j.epsl.2010.07.015>
- Hao, M., Zhang, J. S., Pierotti, C. E., Ren, Z., & Zhang, D. (2019). High-Pressure single-crystal elasticity and thermal equation of state of omphacite and their implications for the seismic properties of eclogite in the Earth's interior. *Journal of Geophysical Research: Solid Earth*, 124(3), 2368–2377. <https://doi.org/10.1029/2018jb016964>
- Isaak, D. G., Ohno, I., & Lee, P. C. (2006). The elastic constants of monoclinic single-crystal chrome-diopside to 1,300 K. *Physics and Chemistry of Minerals*, 32(10), 691–699. <https://doi.org/10.1007/s00269-005-0047-9>
- Ito, K., & Kennedy, G. C. (1971). An experimental study of the basalt-garnet granulite-eclogite transition. In *The structure and physical properties of the Earth's crust* (Vol. 14, pp. 303–314). <https://doi.org/10.1029/GM014p0303>
- Kantor, I., Prakapenka, V., Kantor, A., Dera, P., Kurnosov, A., Sinogeikin, S., et al. (2012). BX90: A new diamond anvil cell design for X-ray diffraction and optical measurements. *Review of Scientific Instruments*, 83(12), 125102. <https://doi.org/10.1063/1.4768541>
- Katsura, T., Yoneda, A., Yamazaki, D., Yoshino, T., & Ito, E. (2010). Adiabatic temperature profile in the mantle. *Physics of the Earth and Planetary Interiors*, 183(1–2), 212–218. <https://doi.org/10.1016/j.pepi.2010.07.001>
- Kay, R. W., & Mahburg-Kay, S. (1991). Creation and destruction of lower continental crust. *Geologische Rundschau*, 80(2), 259–278. <https://doi.org/10.1007/bf01829365>
- Kim, D., Kim, T., Lee, J., Kim, Y., Kim, H., & Lee, J. I. (2018). Microfabrics of omphacite and garnet in eclogite from the Lanterman Range, northern Victoria Land, Antarctica. *Geoscience Journal*, 22(6), 939–953. <https://doi.org/10.1007/s12303-018-0055-7>
- Lai, X., Zhu, F., Zhang, J. S., Zhang, D., Tkachev, S., Prakapenka, V. B., & Chen, B. (2020). An Externally-heated diamond anvil cell for synthesis and single-crystal elasticity determination of Ice-VII at high pressure-temperature conditions. *Journal of Visualized Experiments*, 160, e61389. <https://doi.org/10.3791/61389>
- Li, B., & Neuville, D. R. (2010). Elasticity of diopside to 8 GPa and 1073 K and implications for the upper mantle. *Physics of the Earth and Planetary Interiors*, 183(3–4), 398–403. <https://doi.org/10.1016/j.pepi.2010.08.009>
- Long, M. D., & Silver, P. G. (2008). The subduction zone flow field from seismic anisotropy: A global view. *Science*, 319(5861), 315–318. <https://doi.org/10.1126/science.1150809>
- Mainprice, D., Hielscher, R., & Schaefer, H. (2011). Calculating anisotropic physical properties from texture data using the MTEX open-source package. *Geological Society, London, Special Publications*, 360(1), 175–192. <https://doi.org/10.1144/sp360.10>
- Moghadam, R. H., Treppmann, C. A., Stöckert, B., & Renner, J. (2010). Rheology of synthetic omphacite aggregates at high pressure and high temperature. *Journal of Petrology*, 51(4), 921–945. <https://doi.org/10.1093/petrology/egq006>
- Niday, W., & Humphreys, E. (2020). Complex upper mantle anisotropy in the Pacific Northwest: Evidence from SKS splitting. *Earth and Planetary Science Letters*, 540, 116264. <https://doi.org/10.1016/j.epsl.2020.116264>
- Rivers, M., Prakapenka, V., Kubo, A., Pullins, C., Holl, C., & Jacobsen, S. (2008). The COMPRES/GSECARS gas-loading system for diamond anvil cells at the Advanced Photon Source. *High Pressure Research*, 28(3), 273–292. <https://doi.org/10.1080/08957950802333593>
- Royden, L. H., & Husson, L. (2006). Trench motion, slab geometry and viscous stresses in subduction systems. *Geophysical Journal International*, 167(2), 881–905. <https://doi.org/10.1111/j.1365-246X.2006.03079.x>
- Sang, L., & Bass, J. D. (2014). Single-crystal elasticity of diopside to 14 GPa by Brillouin scattering. *Physics of the Earth and Planetary Interiors*, 228, 75–79. <https://doi.org/10.1016/j.pepi.2013.12.011>
- Sang, L., Vanpeteghem, C. B., Sinogeikin, S. V., & Bass, J. D. (2011). The elastic properties of diopside, CaMgSi2O6. *American Mineralogist*, 96(1), 224–227. <https://doi.org/10.2138/am.2011.3674>
- Shen, G., Wang, Y., Dewaele, A., Wu, C., Fratanduono, D. E., Eggert, J., et al. (2020). Toward an international practical pressure scale: A proposal for an IPPS ruby gauge (IPPS-Ruby2020). *High Pressure Research*, 40(3), 299–314. <https://doi.org/10.1080/08957959.2020.1791107>
- Sinogeikin, S. V., & Bass, J. D. (2000). Single-crystal elasticity of pyrope and MgO to 20 GPa by Brillouin scattering in the diamond cell. *Physics of the Earth and Planetary Interiors*, 120(1–2), 43–62. [https://doi.org/10.1016/S0031-9201\(00\)00143-6](https://doi.org/10.1016/S0031-9201(00)00143-6)
- Skelton, R., & Walker, A. M. (2015). The effect of cation order on the elasticity of omphacite from atomistic calculations. *Physics and Chemistry of Minerals*, 42(8), 677–691. <https://doi.org/10.1007/s00269-015-0754-9>
- Stixrude, L., & Lithgow-Bertelloni, C. (2005). Thermodynamics of mantle minerals—I. Physical properties. *Geophysical Journal International*, 162(2), 610–632. <https://doi.org/10.1111/j.1365-246X.2005.02642.x>
- Walker, A. M. (2012). The effect of pressure on the elastic properties and seismic anisotropy of diopside and jadeite from atomic scale simulation. *Physics of the Earth and Planetary Interiors*, 192–193, 81–89. <https://doi.org/10.1016/j.pepi.2011.10.002>

- Wang, Q., Burlini, L., Mainprice, D., & Xu, Z. (2009). Geochemistry, petrofabrics and seismic properties of eclogites from the Chinese continental scientific drilling boreholes in the Sulu UHP terrane, eastern China. *Tectonophysics*, 475(2), 251–266. <https://doi.org/10.1016/j.tecto.2008.09.027>
- Wedepohl, K. H. (1995). The composition of the continental crust. *Geochimica et Cosmochimica Acta*, 59(7), 1217–1232. [https://doi.org/10.1016/0016-7037\(95\)00038-2](https://doi.org/10.1016/0016-7037(95)00038-2)
- Xu, W., Lithgow-Bertelloni, C., Stixrude, L., & Ritsema, J. (2008). The effect of bulk composition and temperature on mantle seismic structure. *Earth and Planetary Science Letters*, 275(1–2), 70–79. <https://doi.org/10.1016/j.epsl.2008.08.012>
- Zhang, J., Green, H. W., & Bozhilov, K. N. (2006). Rheology of omphacite at high temperature and pressure and significance of its lattice preferred orientations. *Earth and Planetary Science Letters*, 246(3–4), 432–443. <https://doi.org/10.1016/j.epsl.2006.04.006>
- Zhang, J. S., Bass, J. D., Taniguchi, T., Goncharov, A. F., Chang, Y. Y., & Jacobsen, S. D. (2011). Elasticity of cubic boron nitride under ambient conditions. *Journal of Applied Physics*, 109(6), 063521. <https://doi.org/10.1063/1.3561496>
- Zhang, J. S., Bass, J. D., & Zhu, G. (2015). Single-crystal Brillouin spectroscopy with CO₂ laser heating and variable q. *Review of Scientific Instruments*, 86(6), 063905. <https://doi.org/10.1063/1.4922634>

References From the Supporting Information

- Arimoto, T., Gréaux, S., Irifune, T., Zhou, C., & Higo, Y. (2015). Sound velocities of Fe₃Al₂Si₃O₁₂ almandine up to 19 GPa and 1700 K. *Physics of the Earth and Planetary Interiors*, 246, 1–8. <https://doi.org/10.1016/j.pepi.2015.06.004>
- Chen, T., Liebermann, R. C., Zou, Y., Li, Y., Qi, X., & Li, B. (2017). Tracking silica in Earth's upper mantle using new sound velocity data for coesite to 5.8 GPa and 1073 K. *Geophysical Research Letters*, 44(15), 7757–7765. <https://doi.org/10.1002/2017GL073950>
- Fei, Y. (1995). Thermal expansion. In T. J. Ahrens (Ed.), *Mineral physics & crystallography: A handbook of physical constants* (Vol. 2, pp. 29–44). American Geophysical Union.
- Gwanmesia, G. D., Wang, L., Heady, A., & Liebermann, R. C. (2014). Elasticity and sound velocities of polycrystalline grossular garnet (Ca₃Al₂Si₃O₁₂) at simultaneous high pressure and high temperatures. *Physics of the Earth and Planetary Interiors*, 228, 80–87. <https://doi.org/10.1016/j.pepi.2013.09.010>
- Hao, M., Zhang, J. S., Pierotti, C. E., Zhou, W. Y., Zhang, D., & Dera, P. (2020). The seismically fastest chemical heterogeneity in the Earth's deep upper mantle—Implications from the single-crystal thermoelastic properties of jadeite. *Earth and Planetary Science Letters*, 543, 116345. <https://doi.org/10.1016/j.epsl.2020.116345>
- Hill, R. (1963). Elastic properties of reinforced solids: Some theoretical principles. *Journal of the Mechanics and Physics of Solids*, 11(5), 357–372. [https://doi.org/10.1016/0022-5096\(63\)90036-X](https://doi.org/10.1016/0022-5096(63)90036-X)
- Irifune, T., Higo, Y., Inoue, T., Kono, Y., Ohfuji, H., & Funakoshi, K. (2008). Sound velocities of majorite garnet and the composition of the mantle transition region. *Nature*, 451(7180), 814. <https://doi.org/10.1038/nature06551>
- Kandelin, J., & Weidner, D. J. (1988). Elastic properties of hedenbergite. *Journal of Geophysical Research*, 93(B2), 1063–1072. <https://doi.org/10.1029/JB093iB02p01063>
- Kulik, E., Murzin, V., Kawaguchi, S., Nishiyama, N., & Katsura, T. (2018). Thermal expansion of coesite determined by synchrotron powder X-ray diffraction. *Physics and Chemistry of Minerals*, 45, 873–881. <https://doi.org/10.1007/s00269-018-0969-7>
- Li, B., & Neuville, D. R. (2010). Elasticity of diopside to 8 GPa and 1073 K and implications for the upper mantle. *Physics of the Earth and Planetary Interiors*, 183(3–4), 398–403. <https://doi.org/10.1016/j.pepi.2010.08.009>
- Liu, J., Chen, G., Gwanmesia, G. D., & Liebermann, R. C. (2000). Elastic wave velocities of pyrope-majorite garnets (Py₆₂Mj₃₈ and Py₅₀Mj₅₀) to 9 GPa. *Physics of the Earth and Planetary Interiors*, 120(1–2), 153–163. [https://doi.org/10.1016/S0031-9201\(00\)00152-7](https://doi.org/10.1016/S0031-9201(00)00152-7)
- Lu, C., Mao, Z., Lin, J. F., Zhuravlev, K. K., Tkachev, S. N., & Prakapenka, V. B. (2013). Elasticity of single-crystal iron-bearing pyrope up to 20 GPa and 750 K. *Earth and Planetary Science Letters*, 361, 134–142. <https://doi.org/10.1016/j.epsl.2012.11.041>
- Nishihara, Y., Nakayama, K., Takahashi, E., Iguchi, T., & Funakoshi, K. I. (2005). P-V-T equation of state of stishovite to the mantle transition zone conditions. *Physics and Chemistry of Minerals*, 31(10), 660–670. <https://doi.org/10.1007/s00269-004-0426-7>
- Reichmann, H. J., Sinogeikin, S. V., Bass, J. D., & Gasparik, T. (2002). Elastic Moduli of Jadeite-Enstatite Majorite. *Geophysical Research Letters*, 29(19). <https://doi.org/10.1029/2002GL015106>
- Sinogeikin, S. V., & Bass, J. D. (2002). Elasticity of Majorite and a Majorite-Pyrope solid solution to high pressure: Implications for the Transition Zone. *Geophysical Research Letters*, 29(2). <https://doi.org/10.1029/2001GL013937>
- Suzuki, I., & Anderson, O. L. (1983). Elasticity and thermal expansion of a natural garnet up to 1,000 K. *Journal of Physics of the Earth*, 31(2), 125–138. <https://doi.org/10.4294/jpe.1952.31.125>
- Wang, Q., Burlini, L., Mainprice, D., & Xu, Z. (2009). Geochemistry, petrofabrics and seismic properties of eclogites from the Chinese Continental Scientific Drilling boreholes in the Sulu UHP terrane, eastern China. *Tectonophysics*, 475(2), 251–266. <https://doi.org/10.1016/j.tecto.2008.09.027>
- Yang, R., & Wu, Z. (2014). Elastic properties of stishovite and the CaCl₂-type silica at the mantle temperature and pressure: An ab initio investigation. *Earth and Planetary Science Letters*, 404, 14–21. <https://doi.org/10.1016/j.epsl.2014.07.020>